Received 25 August 2022; revised 11 October 2022; accepted 26 October 2022. Date of publication 31 October 2022; date of current version 9 November 2022.
The review of this article was arranged by Editor S. Menzel.

Digital Object Identifier 10.1109/JEDS.2022.3218004

Improved Ferroelectricity in Cryogenic Phase Transition of $Hf_{0.5}Zr_{0.5}O_2$

YIFAN XING [1] (Graduate Student Member, IEEE), YU-RUI CHEN [1] (Graduate Student Member, IEEE), JER-FU WANG [1], ZEFU ZHAO [1] (Graduate Student Member, IEEE), YUN-WEN CHEN [1], GUAN-HUA CHEN [2] (Graduate Student Member, IEEE), YUXUAN LIN [1], RACHIT DOBHAL [3], AND C. W. LIU [4] (Fellow, IEEE)

1 Graduate Institute of Electronics Engineering, National Taiwan University, Taipei 10617, Taiwan
2 Graduate Institute of Photonics and Optoelectronics, National Taiwan University, Taipei 10617, Taiwan
3 Graduate School of Advanced Technology, National Taiwan University, Taipei 10617, Taiwan
4 Department of Electrical Engineering, the Graduate Institute of Electronics Engineering, the Graduate Institute of Photonics and Optoelectronics, and the Graduate School of Advanced Technology, National Taiwan University, Taipei 10617, Taiwan

CORRESPONDING AUTHOR: C. W. LIU (e-mail: chee@cc.ee.ntu.edu.tw; cliu@ntu.edu.tw)

This work was supported in part by the National Science and Technology Council under Grant 111-2622-8-A49-018-SB, Grant 111-2218-E-002-040-MBK, Grant 111-2634-F-A49-008, and Grant 111-2622-8-002-001; and in part by the Ministry of Education under Grant NTU-CC-111L892001.

ABSTRACT Cryogenic transition from metastable tetragonal phase (t-phase) to orthorhombic phase (o-phase) is crucial in achieving the desired ferroelectric characteristics. Observing the reversible transition from anti-ferroelectricity (AFE) to ferroelectricity (FE) in electrical characteristics, the cryogenic phase transition is experimentally analyzed in $Hf_{0.5}Zr_{0.5}O_2$ alloys. Furthermore, the stabilized o-phase formation is more favorable when applying cryogenics to superlattice $Hf_{0.5}Zr_{0.5}O_2$, manifesting a 23% increase in remanent polarization (P_r) at 77K. To theoretically clarify the emergence of phase transition with decreasing temperatures, Landau–Ginzburg–Devonshire theory and first-principle study are combined in this work. Based on the detailed calculation, the increasing relative free energy of the t-phase contributes to lowering the energy barrier when decreasing the temperature, making the convenient transitional pathway from metastable t- to o-phase. This work exhibits the cryogenic phase transition model involving t- and o-phases in $Hf_{0.5}Zr_{0.5}O_2$ and presents a method to boost ferroelectricity for emerging HfO_2-based cryo-device.

INDEX TERMS Ferroelectric (FE), anti-ferroelectric (AFE), low temperature, cryogenic phase transition, high remanent polarization, superlattices.

I. INTRODUCTION

Excellent ferroelectricity demonstrated in the doped-HfO_2 mixtures [1] shed light on emerging non-volatile memories [2], [3], [4] with CMOS compatibility [5]. The evolution toward cryo-CMOS circuits and quantum computing systems may lead to the need of cryogenic non-volatile ferroelectric (Fe) memory [6]. Our recent work demonstrated the $Hf_xZr_{1-x}O_2$ could be applied as a high-κ dielectric due to its anti-ferroelectric (AFE) property [7]. To achieve expected strong ferroelectricity, a high proportion of orthorhombic phase (o-phase) is demanded. It was reported that the formation of o-phase results in FE properties in $Hf_xZr_{1-x}O_2$ thin films by thermal process [8], [9]. It has been visualized that the metastable o-phase appears in the cooling down stage, heating up to the high crystallization temperature and then cooling to room temperature [10]. The amount of crystalline phases like dielectric (DE) monoclinic phase (m-phase), FE o-phase, and AFE tetragonal phase (t-phase) determine the electrical characterizations of $Hf_xZr_{1-x}O_2$. Hence high [Hf] and high [Zr] layer favor FE o-phase and AFE t-phase [11], respectively. It has been reported that o-phase can be stabilized in a particular thickness by tuning the surface energy effect [12]. In addition, our previous work has discussed the effects of oxygen vacancy concentration [V_o] on phase formation [13]. The amount of [V_o] is used to control FE and AFE characteristics at room temperature in our MFM/MIM heterostructures [13]. High [V_o] leads to alloys and favors the AFE characteristics at room temperature, while low

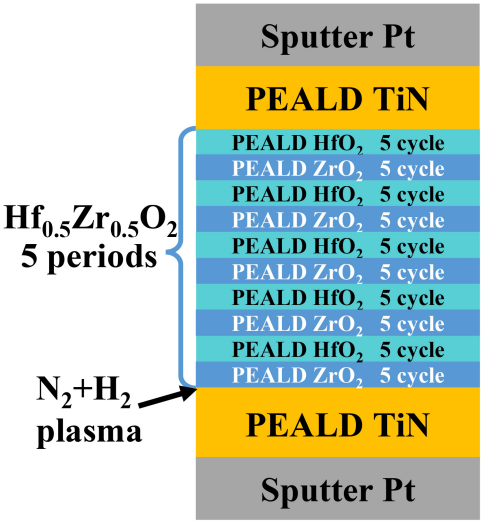

FIGURE 1. Schematic of sputtered Pt/PEALD TiN/PEALD $Hf_{0.5}Zr_{0.5}O_2$ (5 periods)/PEALD TiN/sputtered Pt stacks.

$[V_o]$ leads to superlattices and favors the FE characteristics at room temperature. Furthermore, $Hf_xZr_{1-x}O_2$ with superlattice structures have also been concluded in favoring o-phase, while $Hf_xZr_{1-x}O_2$ alloys helped the formation of t-phase with relatively high dielectric constant [13]. Due to the overlaps of the peak position in grazing incident X-ray diffraction (GIXRD) spectra, the o-phase and t-phase are challenging to be identified in the $Hf_xZr_{1-x}O_2$ films. However, the phase transition can be confirmed thanks to the variations in remanent polarization (P_r) values. The density functional theory (DFT) models for interfacial energy calculation were also reported in [14].

The cryogenic phase transition model is introduced in this work to explain the o-phase transition from t-phase during cooling, validated by the experimental results. The phase transition occurs below Curie temperature, which is also fitted by Landau–Ginzburg–Devonshire (LDG) theory. Kinetics is described by the predicted free energies of the m-, o-, and t-phases by the DFT study as well as the barrier energies of phase transition.

II. EXPERIMENTS

The MFM capacitors were fabricated on Si substrates by Pt/TiN/$Hf_{0.5}Zr_{0.5}O_2$/TiN/Pt (Fig. 1) to investigate the cryogenic transition between t- and o-phase. The bottom sputtered Pt acts as etch-stop and probe layers [15], [16]. The temperature of 250°C was maintained during the plasma-enhanced atomic layer deposition (PEALD) process. The O_2 exposure times of 5s and 10s were used to form alloy and superlattice structures, respectively [13]. The $Hf_{0.5}Zr_{0.5}O_2$ films were made of 5 cycles ZrO_2 and 5 cycles HfO_2 (5 periods, total 10 cycles) (Fig. 1 (a)) while ZrO_2 as the first layer can achieve the higher $2P_r$ than HfO_2 first [13]. The *in-situ* TiN bottom and top electrodes were deposited through PEALD in the forming gas ($50\%N_2 + 50\%H_2$). Note

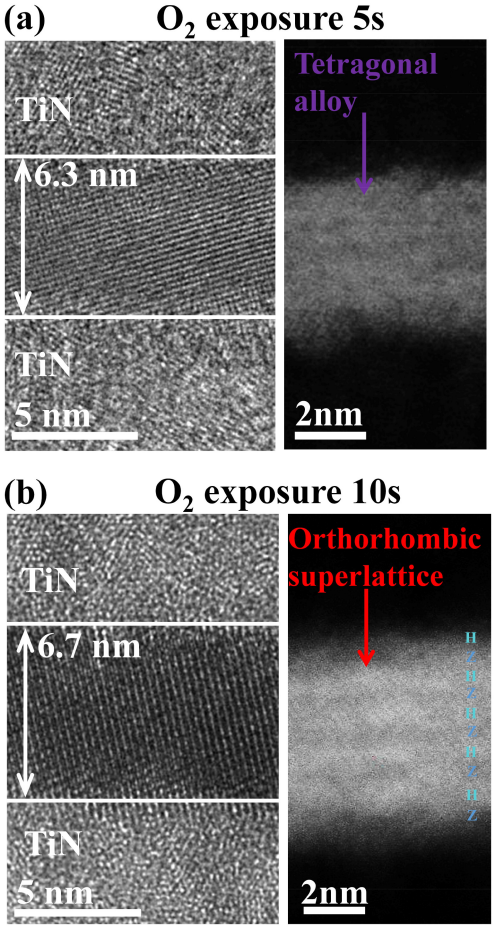

FIGURE 2. TEM and HAADF images with O_2 exposure time of (a) 5s and (b) 10s.

that the precursors of ZrO_2, HfO_2, and TiN are TDMAZr, TDMAHf, and TDMATi, respectively. After the PEALD process of TiN/$Hf_{0.5}Zr_{0.5}O_2$/TiN/Pt (bottom), the top sputtered Pt passivation layer was deposited to avoid the oxidation on TiN surface and patterned by the lift-off process. The TiN/$Hf_{0.5}Zr_{0.5}O_2$/TiN films were etched till bottom Pt layer via reactive ion etching (RIE). After the above processes for device fabrication, the 450°C and 400°C post metallization annealing (PMA) was performed in forming gas ($90\%N_2+10\%H_2$) for the crystallization of the O_2 5s and O_2 10s $Hf_{0.5}Zr_{0.5}O_2$ thin films, respectively.

III. RESULTS AND DISCUSSION

Good crystallinity of the 6.3nm $Hf_{0.5}Zr_{0.5}O_2$ with 5s O_2 exposure is observed by transmission electron microscope (TEM) image (Fig. 2(a)). The $Hf_{0.5}Zr_{0.5}O_2$ film is an alloy with the ZrO_2-HfO_2 interfacial mixture, as shown in the high-angle annular dark-field (HAADF) image. On the other hand, the 6.7 nm $Hf_{0.5}Zr_{0.5}O_2$ with 10s O_2 exposure has high crystallinity in the superlattices with clear ZrO_2-HfO_2 interfaces, as shown in the dark-bright fringes of HAADF (Fig. 2(b)). All the following electrical characteristics are measured from pristine samples.

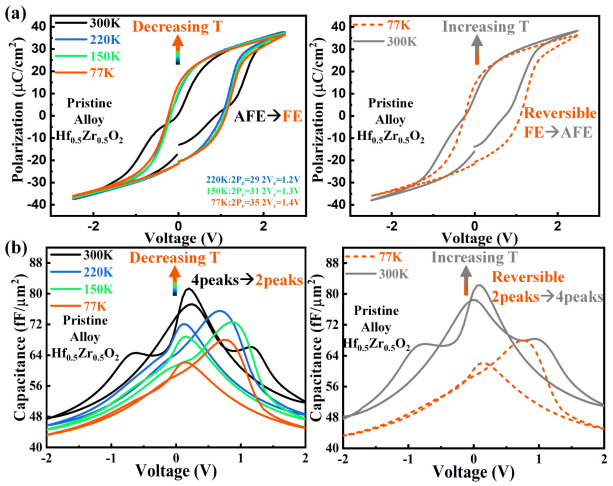

FIGURE 3. (a) P-V loops and (b) C-V curves of $Hf_{0.5}Zr_{0.5}O_2$ alloys with O_2 exposure 5s measured at 300K, 220K, 150K, 77K, and 300K (heating up).

The $Hf_{0.5}Zr_{0.5}O_2$ with 5s O_2 exposure yielded an AFE P-V loop at 300K (Fig. 3(a)), indicating the high [V_o] and alloy structure favored t-phase. Since the free energy of t-, m-, and o-phase is related to the temperature, electrical characteristics can transform when the sample is cooling down to cryogenic temperature [17], [18]. The P-V loop exhibits FE property when the temperature is lowered to 220K, as illustrated in Fig. 3(a). Furthermore, continually lowering the temperatures to 150K and 77K, the FE P-V loops maintain their stability and sustain a rise in $2P_r$ values. Afterward, the P-V loop demonstrates a reversible transition from FE to AFE when heating up to 300K after cooling. To validate the trend of transition from AFE to FE during cooling, C-V sweeps were also measured at 300K, 220K, 150K, 77K, and 300K (heating up after cooling) (Fig. 3(b)). At 300K, t-phase characteristics are consistently demonstrated with 4 peaks in the forward and reverse C-V sweeps [19]. A transition from AFE (4 peaks) to FE (2 peaks) in C-V hysteresis is observed during cooling, coherent with the observation in P-V loops. When the temperature is back to room temperature, the 5s exposure sample shows the AFE P-V loop with 4 peaks in the C-V hysteresis. The reversible transitions from AFE to FE to AFE verify the feasibility that the energy barrier between o- and t-phase can be overcome reversibly. However, to the best of our knowledge, the AFE-FE-AFE transition has not been engineered for applications.

Concerning the observed enhancement of ferroelectricity in low temperatures, we fabricated $Hf_{0.5}Zr_{0.5}O_2$ thin film with O_2 exposure 10s to further investigate the t- to o-phase transition for ferroelectric improvement in cryogenic temperatures. Due to o-phase favoring low [V_o] and superlattices, the pristine P-V loop at 300K shows FE characteristics. Furthermore, the stable FE P-V loop and the higher $2P_r$ are obtained at 77K (54 μC/cm^2) with 23% improvement (Fig. 4(a)), exhibiting the enhanced o-phase amount from transitioned t-phase. Meanwhile, the coercive voltage (V_c) shows an increment as the temperature

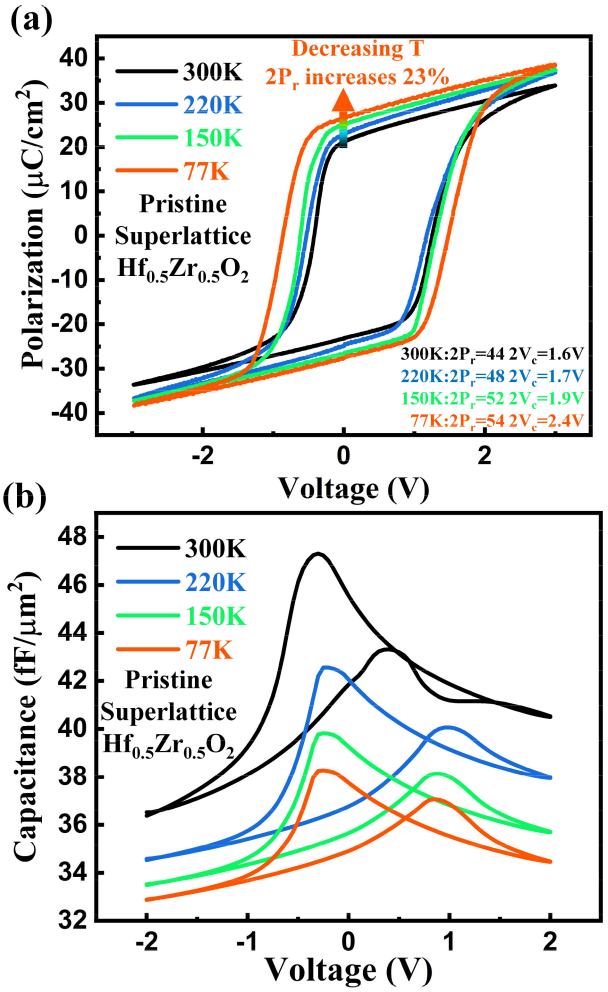

FIGURE 4. (a) P-V loops and (b) C-V curves of $Hf_{0.5}Zr_{0.5}O_2$ superlattices with O_2 exposure 10s measured at 300K, 220K, 150K, and 77K.

decreases [20]. Besides, the C-V hysteresis remain the same with two peaks, indicating ferroelectric dominance during cooling (Fig. 4(b)) [19]. In accordance with the transition of electrical properties from AFE to FE observed in Fig. 3(a) and (b), the cooling process can be a method of lessening t-phase and increasing o-phase to enhance the ferroelectricity. Meanwhile, the high O_2 exposure time 10s achieves the higher P_r value at 77K than our previous work at room temperature [13].

Based on Landau-Ginzburg-Devonshire theory, intrinsic switching is applied to explain the temperature-dependent phase transition [21]. The thermodynamic free energy (G) is an expansion of the polynomial of polarization (P) up to the sixth order,

$$G(T) = \frac{\alpha(T)}{2}P^2 + \frac{\beta}{4}P^4 + \frac{\gamma}{6}P^6 - PE, \quad (1)$$

where α represents the reciprocal of the dielectric susceptibility, β and γ are temperature-independent Landau coefficients, and E is electric field. Relying on this approximation, α is linearly relative to temperature. The reversible

phase transition between the o- and t-phase takes place below the Curie temperature (T_{curie}). On this basis, an expansion of the energy polynomial to the fourth order can be simplified and rewritten. Negative α keeps the sign under the Curie temperature and ranges with decreasing temperatures. The electric field across the ferroelectric at the thermal equilibrium state can be calculated by a differential formula ($\partial G / \partial P = 0$) based on Eq. (1)

$$E = \alpha P + \beta P^3. \tag{2}$$

Known as LGD theory, Eq. (2) offers a simplified description of polarization hysteresis with two crucial coefficients related to phase transitions. Supported by the experimental data P_r and V_c, the intrinsic switching model can be proposed with the coefficients α and β. The value of remanent polarization can be found by setting $E = 0$, revealing:

$$P = \sqrt{\frac{-\alpha}{\beta}}. \tag{3}$$

And, according to the free energy description, following with the Curie-Weiss behavior, the coefficient α:

$$\alpha = \alpha_0 (T - T_{curie}) \tag{4}$$

where α_0 is a positive constant. To determinate the coercive field (E_c), the electric field at local extremes need to be analyzed,

$$E_C = \pm \frac{2}{3} \alpha_0 (T - T_{curie}) \sqrt{\frac{-\alpha_0 (T - T_{curie})}{3\beta}} \tag{5}$$

Applying Eqs. (3) and (5), α_0 and β can be extracted from the experimental data of $Hf_{0.5}Zr_{0.5}O_2$. Considering the gradual transition from AFE to FE spanning between 300K and 220K in $Hf_{0.5}Zr_{0.5}O_2$ with 5s O_2 exposure, AFE data are removed from the following LGD analysis [22]. With the steady growth of P_r during cooling, an enhancement of ferroelectricity is obtained due to the t-phase transition to o-phase (Fig. 5(a)). Note that the Curie temperature of $Hf_{0.5}Zr_{0.5}O_2$ with 5s O_2 exposure is 622K, obtained by the best fit of the LGD model using our experimental data in Fig. 5. Moreover, the continually enhanced ferroelectricity drives the increase of average coercive voltage (V_c) during cooling (Fig. 5(b)).

Confirming the consideration of LGD theory, the $Hf_{0.5}Zr_{0.5}O_2$ with 10s O_2 exposure is performed to further understand the improvement of ferroelectricity by t- to o-phase transition. The Curie temperature is 732K by the best fit of the LGD model using our experimental data in Fig. 6, in line with what has been reported for the similar $Hf_xZr_{1-x}O_2$ system [18], [23], [24], [25]. Compared the estimated α_0 (1.7E6 $VmK^{-1}C^{-1}$) from temperature-dependent permittivity (ε_r) in Curie-Weiss law (Eq. (6)),

$$\varepsilon_r = \frac{\partial E}{\partial P} = \frac{1}{\alpha_0 \ (T_{curie} - T) + 3\beta P^2} \tag{6}$$

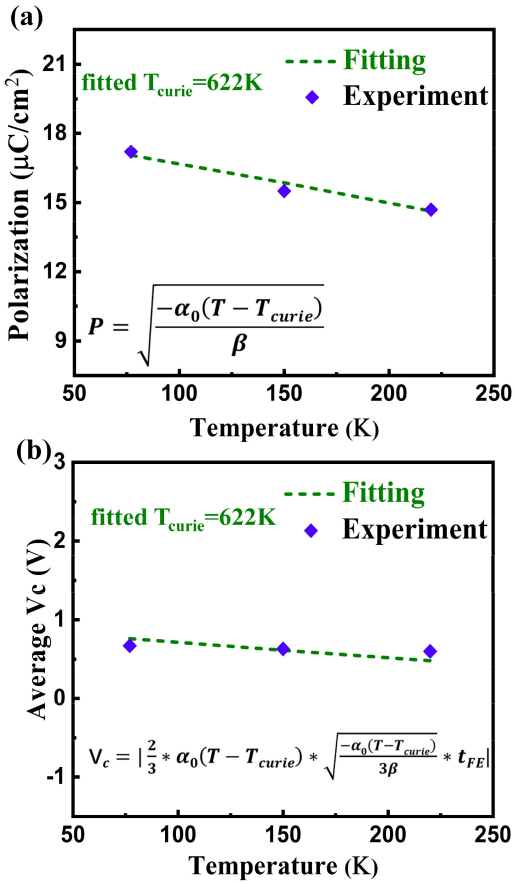

FIGURE 5. Fitting results using the LGD model from $Hf_{0.5}Zr_{0.5}O_2$ alloys with O_2 exposure 5s of (a) remanent polarization and (b) average coercive voltage vs temperatures.

the fitted α_0 (2.7E6 $VmK^{-1}C^{-1}$) from our data by LGD theory is reasonably close. Note that due to the hysteresis in capacitance-voltage measurement (Fig. 4 (b)), the dielectric constant is measured at low voltage without hysteresis. Since the fewer [V_o] occurs in the $Hf_{0.5}Zr_{0.5}O_2$ with O_2 exposure 10s compared with that in the $Hf_{0.5}Zr_{0.5}O_2$ with O_2 exposure 5s, the T_{curie} undergoes an increase [18]. P_r also obtains an improvement of 23% from 300K to 77K (Fig. 6(a)). The low energy barrier from t- to o-phase can obtain more o-phase as temperature decreases. Meanwhile, the fitting average V_c is also aligned with the linear trend (Fig. 6(b)), increased by ferroelectric enhancement [26], [27]. Taking advantage of high V_c, the cryogenic temperature also effectively compensates the loss of memory window (MW $\approx 2V_c$) caused by the thin film [26], [27]. T_{curie} is crucial for the FE o-phase formation during the cooling stage. The amount of [V_o] can be reduced in fabrication to seek a higher T_{curie} and to favor more o-phase formation. Although the LGD theory can illustrate the cryogenic phase transition in properties, the intrinsic phase transition mechanism could not be included due to the lack of energy barriers. The kinetic energy barriers between each phase are critical for understanding the physical mechanism in cryogenics from our experimental data.

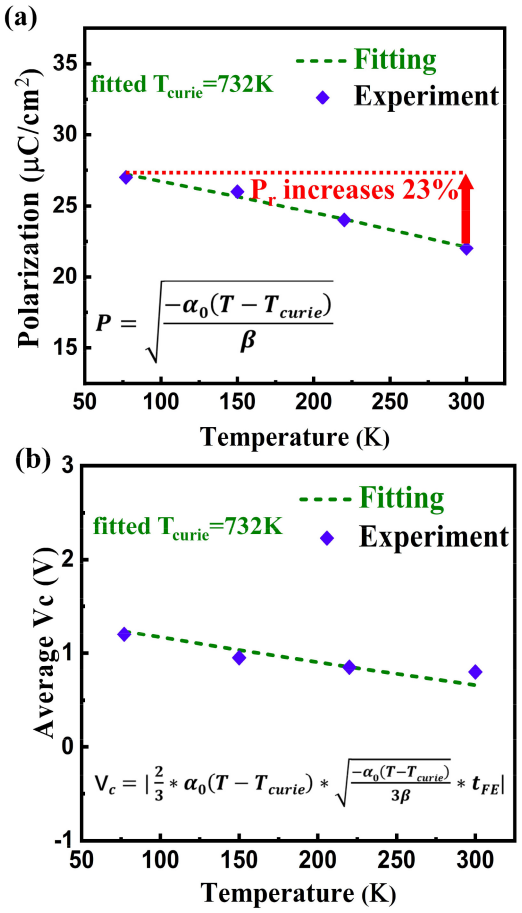

FIGURE 6. Fitting results using the LGD model from $Hf_{0.5}Zr_{0.5}O_2$ superlattices with O_2 exposure 10s of (a) remanent polarization and (b) average coercive voltage vs temperature.

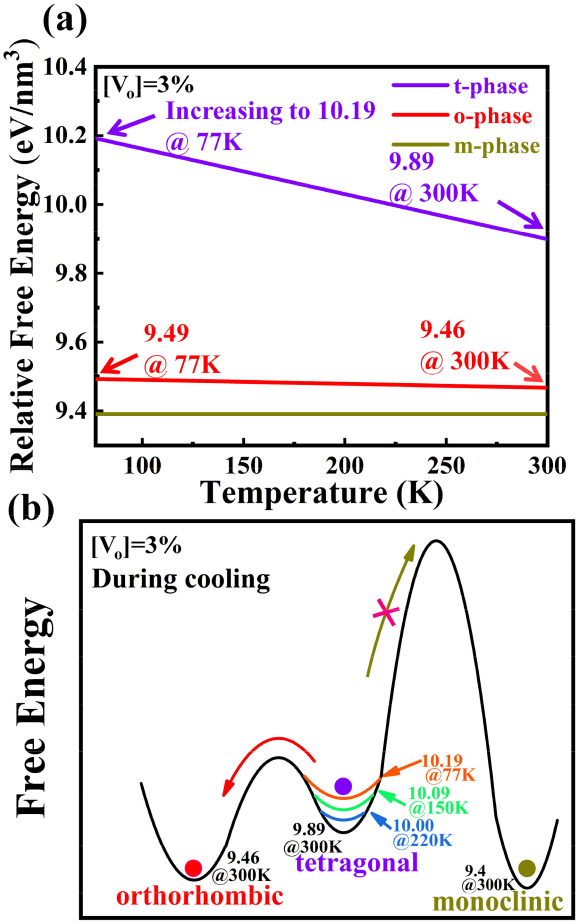

FIGURE 7. (a) Relative free energy of o-, t-, and m-phase with [V_o] = 3% under various temperatures. (b) Schematic diagram of free energy for the phase transition during cooling process. The relative barrier height between o- and t-phase decreases with decreasing temperature, indicating the transition from t-phase to o-phase is more favorable.

To better comprehend, the relative free energies of t-, o-, and m-phase in $Hf_{0.5}Zr_{0.5}O_2$ dependent on temperature are calculated (Fig. 7(a)). Considering the purpose of ferroelectric enhancement, the $Hf_{0.5}Zr_{0.5}O_2$ with 5s O_2 exposure is taken as a reference of theoretical calculation, same as our analyses in LGD fitting. The phase free energy (Eq. (7)) is composed of bulk energy, entropy contribution, and interfacial energy (Eq. (8)) [28], [29].

$$G_i = U_i - TS_i + \Gamma_i \tag{7}$$

$$\Gamma_i = \frac{2\pi\left(r^2 \times \sigma_i + rd \times \delta_i\right)}{\pi r^2 d} \tag{8}$$

Here index i represents the phase in $Hf_{0.5}Zr_{0.5}O_2$ film which could be m-phase, o-phase, or t-phase. G_i, U_i, S_i, and Γ_i are phase free energy, relative bulk energy, entropy, and interfacial energy. For the computational convenience, the relative bulk energy of m-phase is taken as zero. According to the assumption of cylindrical grain grown in $Hf_{0.5}Zr_{0.5}O_2$ film, the interfacial energy Γ_i is a function of interfacial energy of $Hf_{0.5}Zr_{0.5}O_2$/ILs (σ_i) (Table 1), estimated radius of grain size according to experimental $Hf_{0.5}Zr_{0.5}O_2$ ($r \approx 6$nm) [30], thickness of $Hf_{0.5}Zr_{0.5}O_2$ ($d = 6.3$nm),

TABLE 1. Interfacial energies of HZO/ILs [28].

Interfacial Energies of HZO/ILs (J/m^2)	α-HfO_2 (δ_i)	TiN (σ_i)
m-phase	1.17	3.25
o-phase	1.52	3.03
t-phase	0.82	3.00

and crystalline phase/ amorphous $Hf_{0.5}Zr_{0.5}O_2$ interfacial energy (δ_i) (Table 1), as shown in Eq. (8). Note that the grain size radius ($r \approx 6$nm) is assumed accord to the experimental thickness. The G_i, U_i, S_i, and Γ_i are calculated in DFT [28], [29]. The value of Γ_i in our calculation is 9.58 eV/nm^3 for m-phase, 8.45 eV/nm^3 for o-phase, and 7.54 eV/nm^3 for t-phase. The t-phase stability decreases with decreasing temperature due to its increasing free energy.

TABLE 2. Activation barriers between t/m phase and t/o-phase.

t/m-phase	w/o capping	45 meV f.u.$^{-1}$ [31]	315 meV f.u.$^{-1}$ [9]	208 meV f.u.$^{-1}$ [32]
	capping	1.2 eV f.u.$^{-1}$ [33]	2.14 eV f.u.$^{-1}$ [34]	
t/o-phase	w/o capping	30 meV f.u.$^{-1}$ [9]	20 meV f.u.$^{-1}$ [36]	27 meV f.u.$^{-1}$ [37]
	capping	35 meV f.u.$^{-1}$ [38]	23.4 meV f.u.$^{-1}$ [39]	

Based on DFT, the calculated relative free energy can be translated into the free energy landscape (Fig. 7(b)) intuitively with the reported energy barriers of phase transition (Table 2). Note that the explanations from LGD theory exclusively describe the second-order phase transition in phenomenology. The relative free energy(G_i) (Eq. (7), depending on bulk energy(U_i), temperature (T), entropy (S_i), and interfacial energy (Γ_i)) of t-phase keeps increasing while that of other two phases maintain almost static during cooling (Fig. 7(a)). The activation barriers from literatures are listed in Table 2. Due to the much higher energy barrier between t- and m-phase than t- and o-phase (Table 2), t-phase prefers transiting to o-phase instead to m-phase (Fig. 7(b)) [9], [31], [32], [33], [34]. Taking the capping effect into consideration in our samples, the activation barrier between t- and m-phase has a higher value of 1.2 eV f.u.$^{-1}$ [33] to 2.14 eV f.u.$^{-1}$ [34] and suppresses the m-phase formation during the cooling step, similar to [35]. With temperature decreasing from 300K to 77K, the relative free energy of t-phase increases from 9.89 eV/nm^3 to 10.19 eV/nm^3 and the barrier between t- and o-phase decreases (Fig. 7(b)). Therefore, more o-phase is observed at 77K. This mechanism explains the boost of 2Pr viewed in experiments. Furthermore, the lower energy barrier between t- and o-phase (20∼35 meV f.u.$^{-1}$ [9], [36], [37], [38], [39] in Table 2) creates the convenient path for cryogenic phase transition from t- to o-phase. The reversible transition between AFE and FE confirms the activation barrier between t- and o-phase is compatible with KT (26 meV@300K). Most equilibrium can be reached at the experimental temperature.

IV. CONCLUSION

With 23% improvement of $2P_r$, a high value of 54 μC/cm^2 at 77K is obtained, clear cryogenic phase transition in $Hf_{0.5}Zr_{0.5}O_2$ film is elucidated experimentally and theoretically. The increasing relative free energy of t-phase decreases the energy barrier for transforming into o-phase which results in the boost of o-phase contents in $Hf_{0.5}Zr_{0.5}O_2$ film with higher ferroelectricity.

REFERENCES

[1] T. S. Böscke, J. Müller, D. Bräuhaus, U. Schröder, and U. Böttger, "Ferroelectricity in hafnium oxide thin films," *Appl. Phys. Lett.*, vol. 99, no. 10, Sep. 2011, Art. no. 102903, doi: 10.1063/1.3634052.

[2] Y. Goh and S. Jeon, "The effect of the bottom electrode on ferroelectric tunnel junctions based on CMOS-compatible HfO_2," *Nanotechnology*, vol. 29, no. 33, Jun. 2018, Art. no. 335201, doi: 10.1088/1361-6528/aac6b3.

[3] T. Francois et al., "Demonstration of BEOL-compatible ferroelectric $Hf_{0.5}Zr_{0.5}O_2$ scaled FeRAM co-integrated with 130nm CMOS for embedded NVM applications," in *IEDM Tech. Dig.*, Dec. 2019, p. 15, doi: 10.1109/IEDM19573.2019.8993485.

[4] S.-H. Kuk, S.-M. Han, B.-H. Kim, S.-H. Baek, J.-H. Han, and S.-H. Kim, "Comprehensive understanding of the HZO-based n/pFeFET operation and device performance enhancement strategy," in *IEDM Tech. Dig.*, Dec. 2021, p. 33, doi: 10.1109/IEDM19574.2021.9720642.

[5] Q. Luo et al., "A highly CMOS compatible hafnia-based ferroelectric diode," *Nat. Commun.*, vol. 11, no. 1, p. 1391, Dec. 2020, doi: 10.1038/s41467-020-15159-2.

[6] J. Hur, Y.-C. Luo, Z. Wang, S. Lombardo, A. I. Khan, and S. Yu, "Characterizing ferroelectric properties of Hf0.5Zr0.5O2 from deep-cryogenic temperature (4 K) to 400 k," *IEEE J. Explor. Solid-State Comput. Devices Circuits*, vol. 7, no. 2, pp. 168–174, Dec. 2021, doi: 10.1109/JXCDC.2021.3130783.

[7] Y.-R. Chen et al., "ION enhancement of Ge0.98Si0.02 nanowire nFETs by high-κ dielectrics," *IEEE Electron Device Lett.*, vol. 43, no. 10, pp. 1601–1604, Oct. 2022, doi: 10.1109/LED.2022.3201972.

[8] T. Mimura, T. Shimizu, O. Sakata, and H. Funakubo, "Large thermal hysteresis of ferroelectric transition in HfO_2-based ferroelectric films," *Appl. Phys. Lett.*, vol. 118, no. 10, Mar. 2021, Art. no. 112903, doi: 10.1063/5.0040934.

[9] M. H. Park, Y. H. Lee, T. Mikolajick, U. Schroeder, and C. S. Hwang, "Thermodynamic and kinetic origins of ferroelectricity in fluorite structure oxides," *Adv. Electron. Mater.*, vol. 5, no. 3, Dec. 2018, Art. no. 1800522, doi: 10.1002/aelm.201800522.

[10] T. Xin et al., "Atomic visualization of the emergence of orthorhombic phase in $Hf_{0.5}Zr_{0.5}O_2$ ferroelectric film with in-situ rapid thermal annealing," in *Proc. IEEE Symp. VLSI Technol. Circuits (VLSI Technology Circuits)*, 2022, pp. 343–344, doi: 10.1109/VLSITechnologyandCir46769.2022.9830185.

[11] K. Ni et al., "Equivalent oxide thickness (EOT) scaling with hafnium zirconium oxide high-k dielectric near morphotropic phase boundary," in *IEDM Tech. Dig.*, Dec. 2019, p. 7, doi: 10.1109/IEDM19573.2019.8993495.

[12] R. Materlik, C. Künneth, and A. Kersch, "The origin of ferroelectricity in Hf1−xZrxO2: A computational investigation and a surface energy model," *J. Appl. Phys.*, vol. 117, no. 13, Apr. 2015, Art. no. 134109, doi: 10.1063/1.4916707.

[13] Z. Zhao et al., "Engineering $Hf_{0.5}Zr_{0.5}O_2$ ferroelectric/anti-ferroelectric phases with oxygen vacancy and interface energy achieving high remanent polarization and dielectric constants," *IEEE Electron Device Lett.*, vol. 43, no. 4, pp. 553–556, Apr. 2022, doi: 10.1109/LED.2022.3149309.

[14] C. Künneth, R. Materlik, and A. Kersch, "Modeling ferroelectric film properties and size effects from tetragonal interlayer in $Hf_{1-x}Zr_x$ O_2 grains," *J. Appl. Phys.*, vol. 121, no. 20, May 2017, Art. no. 205304, doi: 10.1063/1.4983811.

[15] M. H. Park, H. J. Kim, Y. J. Kim, W. Lee, H. K. Kim, and C. S. Hwang, "Effect of forming gas annealing on the ferroelectric properties of $Hf_{0.5}Zr_{0.5}O_2$ thin films with and without Pt electrodes," *Appl. Phys. Lett.*, vol. 102, no. 11, Mar. 2013, Art. no. 112914, doi: 10.1063/1.4798265.

[16] S. J. Kim et al., "Effect of hydrogen derived from oxygen source on low-temperature ferroelectric TiN/$Hf_{0.5}Zr_{0.5}O_2$/TiN capacitors," *Appl. Phys. Lett.*, vol. 115, no. 18, Aug. 2019, Art. no. 182901, doi: 10.1063/1.5126144.

[17] S. S. Cheema et al., "Ultrathin ferroic HfO_2–ZrO_2 superlattice gate stack for advanced transistors," *Nature*, vol. 604, no. 7904, pp. 65–71, Apr. 2022, doi: 10.1038/s41586-022-04425-6.

[18] U. Schroeder et al., "Temperature-dependent phase transition in $Hf_xZr_{1-x}O_2$ mixed oxides: Indications of a proper ferroelectric material," *Adv. Electron. Mater.*, vol. 8, no. 9, May 2022, Art. no. 2200265, doi: 10.1002/aelm.202200265.

[19] M. H. Lee et al., "Steep slope and near non-hysteresis of FETs with antiferroelectric-like HfZrO for low-power electronics," *IEEE Electron Device Lett.*, vol. 36, no. 4, pp. 294–296, Apr. 2015, doi: 10.1109/LED.2015.2402517.

[20] Y. Zhang et al., "Enhanced ferroelectric properties and insulator–metal transition-induced shift of polarization-voltage hysteresis loop in VO_x -capped $Hf_{0.5}Zr_{0.5}O_2$ thin films," *ACS Appl. Mater. Interfaces*, vol. 12, no. 36, pp. 40510–40517, Sep. 2020, doi: 10.1021/acsami.0c10964.

[21] C. Gastaldi et al., "Intrinsic switching in Si-doped HfO_2: A study of Curie–Weiss law and its implications for negative capacitance field-effect transistor," *Appl. Phys. Lett.*, vol. 118, no.19, Apr. 2021, Art. no. 192904, doi: 10.1063/5.0052129.

[22] P. D. Lomenzo et al., "Universal curie constant and pyroelectricity in doped ferroelectric HfO2 thin films," *Nano Energy*, vol. 74, Aug. 2020, Art. no. 104733, doi: 10.1016/j.nanoen.2020.104733.

[23] T. Shimizu et al., "The demonstration of significant ferroelectricity in epitaxial Y-doped HfO_2 film," *Sci. Rep.*, vol. 6, Sep. 2016, Art. no. 32931, doi: 10.1038/srep32931.

[24] H. Chen et al., "Temperature dependent polarization-switching behavior in $Hf_{0.5}Zr_{0.5}O_2$ ferroelectric film," *Materialia*, vol. 14, Dec. 2020, Art. no. 100919, doi: 10.1016/j.mtla.2020.100919.

[25] T. Mittmann, M. Materano, S.-C. Chang, I. Karpov, T. Mikolajick, and U. Schroeder, "Impact of oxygen vacancy content in ferroelectric HZO films on the device performance," in *IEDM Tech. Dig.*, Dec. 2020, p. 18, doi: 10.1109/IEDM13553.2020.9372097.

[26] Z. Fan, J. Chen, and J. Wang, "Ferroelectric HfO2-based materials for next-generation ferroelectric memories," *J. Adv. Dielectr.*, vol. 6, no. 2, Jun. 2016, Art. no. 1630003, doi: 10.1142/S2010135X16300036.

[27] H. Mulaosmanovic, E. T. Breyer, T. Mikolajick, and S. Slesazeck, "Ferroelectric FETs With 20-nm-Thick HfO2 layer for large memory window and high performance," *IEEE Trans. Electron Devices*, vol. 66, no. 9, pp. 3828–3833, Sep. 2019, doi: 10.1109/TED.2019.2930749.

[28] Y.-T. Tang et al., "A comprehensive study of polymorphic phase distribution of ferroelectric-dielectrics and interfacial layer effects on negative capacitance FETs for Sub-5 nm node," in *Proc. IEEE Symp. VLSI Technol.*, Jun. 2018, pp. 45–46, doi: 10.1109/VLSIT.2018.8510696.

[29] Y.-W. Chen and C. W. Liu, "Boost of orthorhombic population with amorphous SiO_2 interfacial layer—A DFT study," *Semicond. Sci. Technol.*, vol. 37, no. 5, Mar. 2022, Art. no. 05LT01, doi: 10.1088/1361-6641/ac5a5e.

[30] H. J. Kim et al., "Grain size engineering for ferroelectric Hf0.5Zr0.5O2 films by an insertion of Al2O3 interlayer," *Appl. Phys. Lett.*, vol. 105, no. 19, 2014, Art. no. 192903, doi: 10.1063/1.4902072.

[31] J. Wu, F. Mo, T. Saraya, T. Hiramoto, and M. Kobayashi, "A first-principles study on ferroelectric phase formation of Si-doped HfO_2 through nucleation and phase transition in thermal process," *Appl. Phys. Lett.*, vol. 117, no. 25, Dec. 2020, Art. no. 252904, doi: 10.1063/5.0035139.

[32] B. M. Hudak et al. "Real-time atomistic observation of structural phase transformations in individual hafnia nanorods," *Nat. Commun.*, vol. 8, May 2017, Art. no. 15316, doi: 10.1038/ncomms15316.

[33] A. Toriumi, Y. Nakajima, and K. Kita, "Opportunity for phase-controlled higher-k HfO_2" *ECS Trans.*, vol. 41, no. 7, pp. 125–136, 2011, doi: 10.1149/1.3633292.

[34] Y. H. Lee et al., "Nucleation-limited ferroelectric orthorhombic phase formation in $Hf_{0.5}Zr_{0.5}O_2$ thin films," *Adv. Electron. Mater.*, vol. 5, Feb. 2019, no. 1800436, doi: 10.1002/aelm.201800436.

[35] A. Kashir, H. Kim, S. Oh, and H. Hwang, "Large remnant polarization in a wake-up free $Hf_{0.5}Zr_{0.5}O_2$ ferroelectric film through bulk and interface engineering," *ACS Appl. Electron. Mater.*, vol. 3, no. 2, pp. 629–638, 2021, doi: 10.1021/acsaelm.0c00671.

[36] S. E. Reyes-Lillo, K. F. Garrity, and K. M. Rabe, "Antiferroelectricity in thin-film ZrO2 from first principles," *Phys. Rev. B*, vol. 90, no. 14, Oct. 2014, Art. no. 140103, doi: 10.1103/PhysRevB.90.140103.

[37] T. D. Huan, V. Sharma, G. A. Rossetti, and R. Ramprasad, "Pathways towards ferroelectricity in hafnia," *Phys. Rev. B*, vol. 90, Aug. 2014, Art. no. 64111 doi: 10.1103/PhysRevB.90.064111.

[38] S.-J. Chang et al., "Visualizing ferroelectric uniformity of Hf1−xZrxO2 films using X-ray mapping" *ACS Appl. Mater. Interfaces*, vol. 13, no. 24, pp. 29212–29221, 2021, doi: 10.1021/acsami.1c08265.

[39] J. W. Adkins, I. Fina, F. Sánchez, S. R. Bakaul, and J. T. Abiade, "Thermal evolution of ferroelectric behavior in epitaxial Hf0.5Zr0.5O2," *Appl. Phys. Lett.*, vol. 117, no. 14, Oct. 2020, Art. no. 142902, doi: 10.1063/5.0015547.